Transient porosity generated at the serpentinization front

Simone Pujatti[1], Benjamin Tutolo[1], Oliver Plümper[2]

[1]University of Calgary, Department of Geoscience, Reactive Transport Group, pujatti.simone@ucalgary.ca

[2]Utrecht University, Department of Earth Sciences, o.plumper@uu.nl

Introduction

Olivine and pyroxene are the main components of peridotites, which are ultramafic rocks widely exposed at mid-ocean ridges, subduction settings and ophiolites. When they interact with seawater under upper lithospheric temperatures, they undergo a hydration reaction that alters them to serpentine minerals and can be represented by chemical equations as:

$$MgSiO_3 + Mg_2SiO_4 + 2H_2O = Mg_3Si_2O_5(OH)_4 \quad (1)$$
$$pyroxene + olivine + water = serpentine$$

$$2Mg_2SiO_4 + 3H_2O = Mg_3Si_2O_5(OH)_4 + Mg(OH)_2 \quad (2)$$
$$olivine + water = serpentine + brucite$$

These reactions involve a solid molar volume increase of up to 50%, corresponding to a density decrease from 3.3 g/cm^3 of a fresh peridotite to ~2.5 g/cm^3 of a completely serpentinized rock (Toft et al., 1990). A density decrease of such magnitude bears strong implications for the rheology and geodynamic behavior of the oceanic lithosphere.

Serpentinization reactions are kinetically fast, thus controlled by the supply of reactants through the rock's porous network. In principle, the volume increase associated with serpentinization should clog any void and stop the reaction, which is in contrast with the observation of natural peridotites that are completely serpentinized (Hopson et al., 1981). Several datasets (Diamantis et al., 2009; Tutolo et al., 2016) suggest that the porosity content of serpentinites increases with the alteration degree (Fig. 1).

Reaction-induced fracturing is a mechanism that can explain the generation of porosity during serpentinization due to a "pressure of crystallization" exerted by growing serpentine crystals in their surroundings. When pressure exceeds the local minimum principal stress, fracturing occurs (Kelemen and Hirth, 2012; Plümper et al., 2012). This mechanism entails a positive feedback between the chemical reaction, which causes a volume expansion that leads to fracturing, and enhanced transport along the newly formed pores, which allows the reaction to proceed to completion. With the present study we aim to identify the presence of pores at the serpentinization front and examine the role that porosity plays in serpentinization reactions.

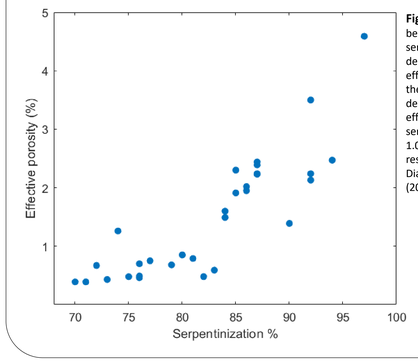

Fig. 1 Relationship between the serpentinization degree and the effective porosity of the rock. The standard deviations of the effective porosity and serpentinization % are 1.03 % and 7.25 %, respectively. Data after Diamantis et al. (2009).

Methods

One thin section made from the Ocean Drilling Program (ODP) core sample 209/1274A/3R/1/61-71 was analysed with a FEI Helios NanoLab™ 660 DualBeam SEM/FIB at Utrecht University (NL) to produce two focused ion beam scansion electron microscopy (FIB-SEM) tomographic datasets:

- **MAR01** – with a voxel resolution of 7.71 nm in the XY directions and 10 nm along Z
- **MAR02** – with a voxel resolution of 1.69 nm in the XY directions and 10 nm along Z

A FIB-SEM apparatus integrates the traditional SEM with an ion gun and a sample stage that can be tilted to obtain an angle of 50° to 60° between the electron beam and a focused ion beam (usually Gallium). The ion beam mills a series of consecutive nanometric slices. After one slice is removed, the system collects a back-scattered electron (BSE) image (Fig. 2). This allows to obtain a stack of 2D images that can be reconstructed in 3D with image processing software. The datasets MAR01 and MAR02 where processed at the University of Calgary with the 3D visualization and data analysis packages Pergeos and ImageJ. Subvolumes of ~ 32 µm^3 and 7 µm^3 were selected respectively from MAR01 and MAR02 to be rendered in 3D for microstructural quantification.

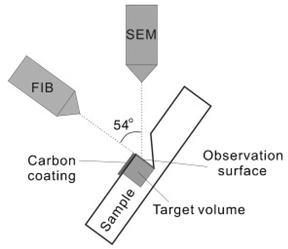

Fig. 2 Schematic representation of the FIB-SEM apparatus. The carbon coating shown in figure is applied with a gas injector. It prevents charging on the surface of the sample, which would generate artefacts in the output images. Gold and platinum are typical materials used in place of carbon. After Iwai et al. (2010).

Results

Legend:
Ol = Olivine; Liz = Lizardite (serpentine polymorph)

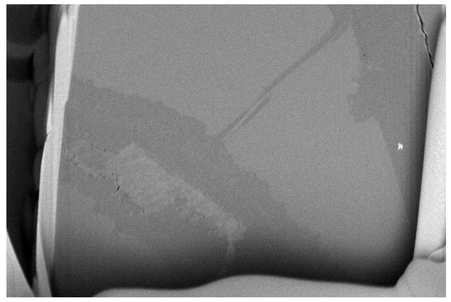

Fig. 3 Dataset MAR01, FIB-SEM image. Dark grey = serpentine, light grey = olivine, bright particle on the right = magnetite. Height of the field of view = 7.893 µm, width = 11.84 µm. The curved bands on the sides and bottom part of the image are made of amorphous material redeposited after the ion milling.

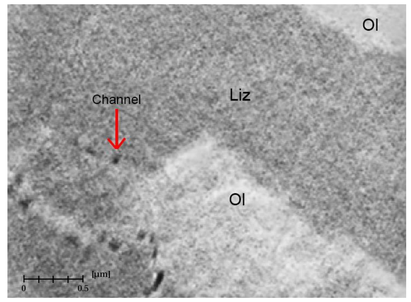

Fig. 4 Dataset MAR01, grey intensity image. Zoom in on the left portion of Fig. 3. The contrast of the image has been enhanced to highlight the microstructures.

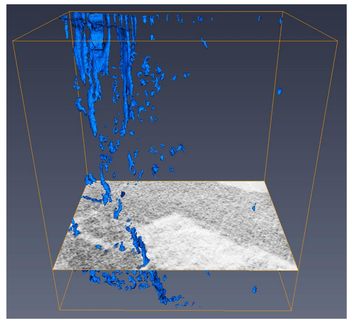

Fig. 5 Dataset MAR01, 3D rendering of the segmented porous network, showing subparallel channels stretching along the z direction. The orthoslice shown in Fig. 4 is displayed to highlight the correspondence between the imaged and segmented pores. The dimensions of the bounding box are 3.38 µm x 2.48 µm x 3.83 µm.

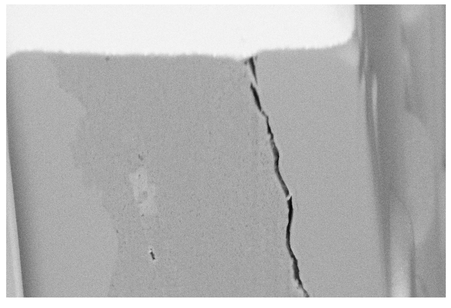

Fig. 6 Dataset MAR02, FIB-SEM image. Dark grey = serpentine, light grey = olivine. Height of the field of view = 3.45 µm, width = 5.18 µm.

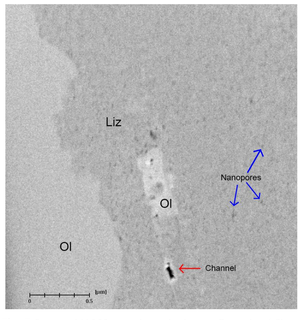

Fig. 7 Dataset MAR02, grey intensity image. Zoom in of Fig. 6. Both the contrast and brightness of the image have been adjusted to reveal the presence of nanopores within the serpentine matrix.

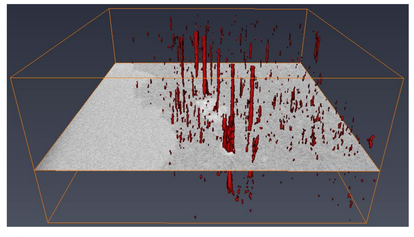

Fig. 8 Dataset MAR02, 3D rendering of the segmented porous network. Subparallel channels are present as in Fig. 5. In addition, this higher-resolution dataset shows a population of smaller nanopores that are scattered in the serpentine matrix and have a preferential orientation parallel to that of the main channels. The orthoslice shown in Fig. 4 is displayed to highlight the correspondence between the imaged and segmented pores. The dimensions of the bounding box are 2.45 µm x 2.55 µm x 1.17 µm.

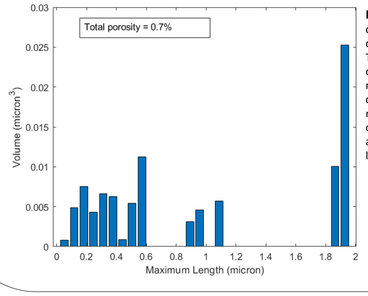

Fig. 9 Pore size distribution of dataset MAR01 (lower resolution dataset). Number of bins = 30. The y axis reports the 3D volume of the pores and the x axis the maximum Feret diameter. The distribution shows at least two main population of pores: channels at high pore's lengths and smaller particles at lower lengths.

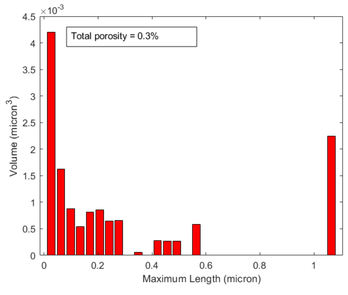

Fig. 10 Pore size distribution of dataset MAR02. Number of bins = 30. The y and x axis are the same as in Fig. 9. The bimodal distribution of pore sizes is more evident than in MAR01. The higher resolution of this second dataset allowed to record the volumetric contribution of the nanoporosity, which accounts for more than twice as much volume as the channeled porosity.

Discussion & Conclusions

The FIB-SEM analysis highlighted the presence of two types of pores:

- A **channeled** wormhole-like porous network found at the reaction front in both datasets (Fig. 4, 7). This porosity shows a preferential orientation parallel to the grain boundaries of the partly replaced olivine. This structure is interpreted as evidence of the **incipient stage** of replacement, entailing that serpentinization is initially dominated by the dissolution of olivine.
- A smaller **nanoporosity** identified in the higher resolution dataset MAR02 (Fig. 7). It is found at a distance from the reaction front and is scattered throughout the fully replaced serpentine matrix. Importantly, it is subparallel to the coarser channeled porosity. It is interpreted as the product of an advanced stage of alteration, when the reaction approaches **equilibrium** and the precipitation of serpentine minerals dominates over dissolution, thus partially clogging the channeled porosity. The nanoporosity represents the remnants of what initially was channeled porosity.

The FIB-SEM data identify nanoporous structures that are evidence of the dynamic evolution and transient nature of porosity in serpentinites. The subparallel orientation of the pores has likely been inherited from a primary crystallographic-preferred orientation (CPO), originally formed as a magmatic texture in the peridotite and subsequently transferred to the alteration products. The latter interpretation bears strong implications for the extent of serpentinization achievable in natural settings, since primary CPOs would control the direction of fluid transport and hence the direction of propagation of the serpentinization front. This hypothesis will be tested in the future by correlating the FIB-SEM datasets presented in this study with EBSD mapping data from the same sample.

The presence of a channelized transient porosity at the reaction front offers insights on the replacement mechanism. However, the total volume fraction of the porosity (0.7% in MAR01; 0.3% in MAR02) is too low to account for the porosity values shown in Fig. 1. It is likely that porosity measurements without a confining pressure produce unrepresentative values, since voids open due to decompression when samples are brought to the surface. This hypothesis will be tested by performing neutron scattering experiments to measure the nanoporosity content of serpentinite samples under a confining pressure.

Acknowledgement

This research used samples and data provided by the International Ocean Discovery Program (IODP). We acknowledge the support of the Natural Sciences and Engineering Research Council of Canada (NSERC) for providing funding for this research. This study would not have been possible without the support of InterRidge, granted through a Graduate Student Fellowship in 2019.

References

Diamantis, K., Gartzos, E., & Migiros, G. (2009). Study on uniaxial compressive strength, point load strength index, dynamic and physical properties of serpentinites from Central Greece: test results and empirical relations. *Engineering Geology*, *108*(3-4), 199-207.

Hopson, C. A., Coleman, R. G., Gregory, R. T., Pallister, J. S., & Bailey, E. H. (1981). Geologic section through the Samail ophiolite and associated rocks along a Muscat-Ibra transect, southeastern Oman Mountains. *Journal of Geophysical Research: Solid Earth*, *86*(B4), 2527-2544.

Iwai, H., Shikazono, N., Matsui, T., Teshima, H., Kishimoto, M., Kishida, R., ... & Muroyama, H. (2010). Quantification of SOFC anode microstructure based on dual beam FIB-SEM technique. *Journal of Power Sources*, *195*(4), 955-961.

Kelemen, P. B., & Hirth, G. (2012). Reaction-driven cracking during retrograde metamorphism: Olivine hydration and carbonation. *Earth and Planetary Science Letters*, *345*, 81-89.

Plümper, O., Røyne, A., Magrasó, A., & Jamtveit, B. (2012). The interface-scale mechanism of reaction-induced fracturing during serpentinization. *Geology*, *40*(12), 1103-1106.

Toft, P. B., Arkani-Hamed, J., & Haggerty, S. E. (1990). The effects of serpentinization on density and magnetic susceptibility: a petrophysical model. *Physics of the Earth and Planetary Interiors*, *65*(1-2), 137-157.

Tutolo, B. M., Mildner, D. F., Gagnon, C. V., Saar, M. O., & Seyfried Jr, W. E. (2016). Nanoscale constraints on porosity generation and fluid flow during serpentinization. *Geology*, *44*(2), 103-106.